OPTICA

Exploring the structure, metabolism, and biochemistry of the neuronal microenvironment label-free using fast simultaneous multimodal optical microscopy

Rishyashring R. Iyer,[1,2] Janet E. Sorrells,[1,3] Lingxiao Yang,[1,2] Carlos A. Renteria,[1,3] Eric J. Chaney,[1] Kayvan F. Tehrani,[1] Darold R. Spillman Jr.,[1] and Stephen A. Boppart[1,2,3,4,5,6,*]

[1]Beckman Institute for Advanced Science and Technology, University of Illinois Urbana-Champaign, Urbana, Illinois 61801, USA
[2]Department of Electrical and Computer Engineering, University of Illinois Urbana-Champaign, Urbana, Illinois 61801, USA
[3]Department of Bioengineering, University of Illinois Urbana-Champaign, Urbana, Illinois 61801, USA
[4]Center for Label-free Imaging and Multiscale Biophotonics (CLIMB), University of Illinois Urbana-Champaign, Urbana, Illinois 61801, USA
[5]Cancer Center at Illinois, University of Illinois Urbana-Champaign, Urbana, Illinois 61801, USA
[6]Carle Illinois College of Medicine, University of Illinois Urbana-Champaign, Urbana, Illinois 61801, USA
*boppart@illinois.edu

Received 18 June 2024; revised 11 August 2024; accepted 25 August 2024; published 19 September 2024

The technologies to examine the neuronal microenvironment label free remain critically underexplored. There is a gap in our knowledge of underlying metabolic, biochemical, and electrophysiological mechanisms behind several neurological processes at a cellular level, which can be traced to the lack of versatile and high-throughput tools to investigate neural networks. In this paper, four label-free contrasts were explored as mechanisms to study neuronal activity, namely, scattering, birefringence, autofluorescence from metabolic cofactors and molecules, and local biochemistry. To overcome challenges of observing neuronal activity spanning three orders of magnitude in space and time, microscopes had to be developed to simultaneously capture these contrasts quickly, with high resolution, and over a large FOV. We developed versatile autofluorescence lifetime, multiharmonic generation, polarization-sensitive interferometry, and Raman imaging in epi-detection (VAMPIRE) microscopy to simultaneously observe multiple facets of neuronal structure and dynamics. The accelerated computational-imaging-driven acquisition speeds, the utilization of a single light source to evoke all contrasts, the simultaneous acquisition that provides an otherwise impossible multimodal dynamic imaging capability, and the real-time processing of the data enable VAMPIRE microscopy as a powerful imaging platform for neurophotonics and beyond.

https://doi.org/10.1364/OPTICA.532367

1. INTRODUCTION

Over a century ago, the neuron doctrine described the nervous system as consisting of a complex network of individual neurons that facilitate communication through the transfer of electrical impulses. Yet, the intricacies of the neuronal environment remain a mystery. This gap can be traced back to the lack of versatile and high-throughput tools to functionally investigate neural networks. Optical microscopy covers the vast spatiotemporal scales of neuronal activity. This paper focuses on establishing multimodal label-free optical tools for observing the activity of the neuronal microenvironment in action in its native state to fill these critical knowledge gaps. Most applications of optical microscopy in neuroimaging have been limited to the use of fluorescent labels or optogenetics. Label-free optical microscopy is less invasive and more versatile, and has a higher potential for future clinical translatability, which leads to the question: what are the label-free markers for the structural and functional dynamics of the neuronal microenvironment?

The ion flux that induces the electrical signals in a cell creates subtle changes to the cell refractive index and the local microenvironment [1,2]. The mechanical action of these ion channels also deforms the cell membrane, which changes the local birefringence [3]. While these changes are subtle, they can be measured using optical interferometry combined with polarization imaging. Second, active neurons have dynamic energy requirements; therefore, they experience rapid changes to their metabolic states. Cell metabolism involves several autofluorescent co-factors like reduced nicotinamide adenine dinucleotide (NADH) and its phosphorylated form (NADPH) or flavin adenine dinucleotide (FAD). Since the fluorescence lifetime of NAD(P)H and FAD are related to the metabolic state of the cells, fast fluorescence lifetime imaging microscopy (FLIM) can track these metabolic changes

in real time [4–6]. There are also local changes to the chemical environment because of neuronal electrical and metabolic activities; vibrational spectroscopy with coherent Raman imaging can characterize these changes rapidly. Measuring these physical and chemical changes using polarization imaging, functional optical coherence microscopy (OCM), FLIM, and Raman scattering microscopy provides an avenue for label-free optical measurement of the electrical activity of neurons.

The metabolism of neurons is critical to their activity and subsequent recovery. Metabolism and energy regulation in the neuronal microenvironment involve several parallel processes, such as the glucose transport and utilization for mitochondrial metabolism in the neurons [7] and supporting glial cells [8], the astrocyte-neuron lactate shuttle [9,10], the metabolism of neurotransmitter synthesis, release, and uptake [11–13], and the energy required to drive the ion pumps to maintain homeostasis [14,15]. Understanding the intricate interplay between these parallel processes is essential for unraveling the complexities of neurometabolism and its implications for brain function and health. Metabolic profiling techniques, such as mass-spectrometry-based metabolomics, allow the comprehensive analysis of small-molecule metabolites in biological samples [16,17]. While radiographic and Raman probes such as 2-deoxyglucose [18] or deuterated glucose [19] can track specific metabolic pathways, they lack the versatility to observe multiple parallel processes. As an alternative to imaging the glucose or lipid consumption, fluorescent redox probes such as dihydroethidium [20], MitoSOX (for mitochondrial oxidative stress) [21,22], or nitroreductase-based probes [23] are used for metabolic imaging of neurons on a cellular scale. Redox pathways are involved in several metabolic processes in the neuronal environment. Most tags are designed to be specific to a small subset of these processes. However, imaging the cellular autofluorescence intensity and lifetime from metabolic co-factors such as NADH and FAD can also report on the redox state of the biological samples [6,24–28] [Fig. 1(a)]. The role of these factors in metabolism, their fluorescence properties, and the utility of FLIM are described in Fig. S1 and Note S1 in Supplement 1.

Due to their lengths and large structures, neuronal metabolism is compartmentalized, including the TCA cycle and the electron transport chain (ETC) in mitochondria, glycolysis related to membrane ion pumping, and glycolysis for pyruvate generation for further aerobic metabolism. Previous studies have explored the change in the NADH and FAD fluorescence intensity [29,30] during electrical activity. A model proposed by Aubert *et al*. [31] suggested a decrease in the NADH levels following activation, followed by a prolonged increase to the overall NADH level before a return to baseline over several dozen seconds. There is also a notable change in the local lactate dehydrogenase (LDH) concentrations in neurons. Astrocytes were shown to not have this initial decrease, but just an increase in response to stimulation of neighboring neurons. There was also an overall increase in the tissue lactate concentrations. This was validated experimentally by Kasischke *et al*. [5] FAD autofluorescence intensity was shown to have the opposite dynamics of NADH in neurons [4,32]. The shuttling of lactate between different cells in the neuronal microenvironment was observed with the Peredox sensor, which is sensitive to the cytosolic NAD^+/NADH ratio [9].

The Raman microscopy method most conducive to being combined with multiphoton imaging is coherent anti-Stokes Raman scattering (CARS) microscopy. However, for hyperspectral information, the detection must either be in the spectral domain or the difference between the pump and Stokes energies must be scanned in time or frequency. The former needs long acquisition times and is not optimal for neuroimaging. The latter is typically achieved using spectral focusing, which needs picosecond-long pump pulses. However, the efficiency of multiphoton fluorescence is severely reduced at picosecond pulse widths. A recent technique called temporally optimized spectrally shaped (TOSS) CARS used

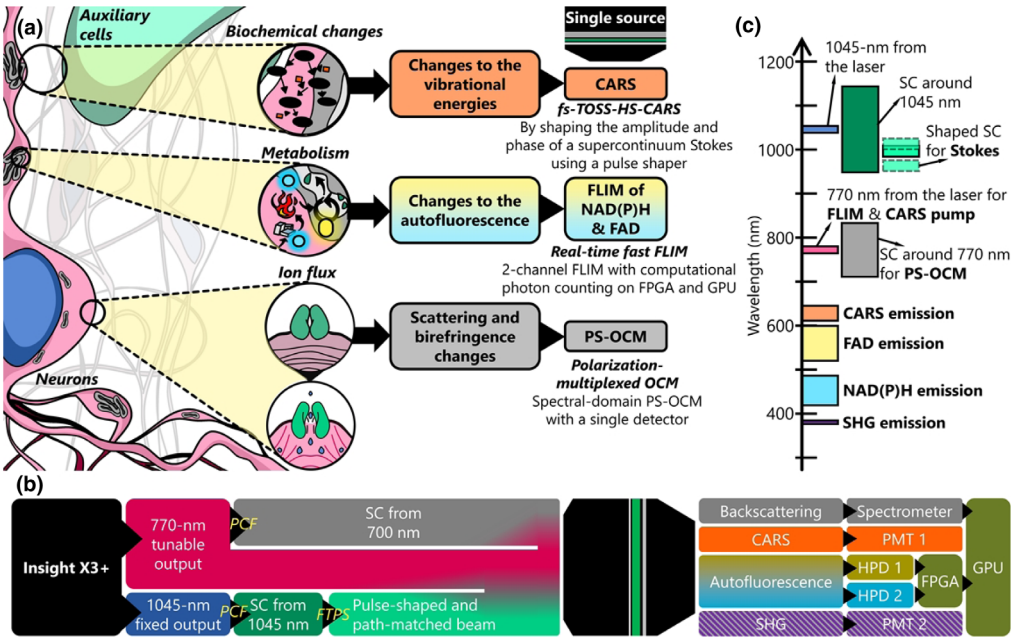

Fig. 1. Contrasts, spectral coverage, and system setup of VAMPIRE microscopy. (a) Illustration of the various physical, metabolic, and biochemical changes in the neuronal microenvironment and how optical microscopy modalities can access these contrasts. (b) Simplified schematic of the single source simultaneous detection in VAMPIRE microscopy. SC: supercontinuum, PCF: photonic crystal fiber, PMT: photomultiplier tube, HPD: hybrid photodetector, FTPS: Fourier transform pulse shaper. (c) Spectral coverage of the excitation and detection in VAMPIRE microscopy, where the colors correspond to the colors of the light paths in (b).

amplitude and phase pulse shaping of a supercontinuum to scan and match different pump and Stokes spectral windows [33,34]. A variant of the technique was described for a femtosecond pump pulse and a shaped supercontinuum Stokes pulse that could scan different spectral windows within the CH stretching region. The CH region has strong signals in biological samples and is useful in imaging and separating protein and lipid components [35]. Considering the abundance of lipids in the brain [36], the addition of CARS to this multimodal scope will unlock new avenues into structural and dynamic imaging of the neuronal environment.

A prevalent technique for label-free imaging of neuronal activity involves optical coherence tomography (OCT) and its corresponding high-resolution variant OCM [1,37–47]. Individual action potentials can be discerned from the light scattered at large angles [48] or by differential detection of the membrane displacements from brightfield microscopy [2]. Even long-term changes to the cellular potential have been tracked by phase-sensitive interferometry [49–51]. Full-field interferometry, quantitative phase imaging, and digital holographic microscopy have also been used to balance the spatiotemporal range of the measured scattered optical field [52–54]. Apart from changes to the refractive index, changes to the local birefringence also report neuronal activity [3,55–57]. Studies also found that changes to the birefringence are larger than the changes to the backscattered light due to axonal reorientation during changing membrane potentials, sometimes up to an order of magnitude [58]. Certain fibers and matrix proteins also have second harmonic generation (SHG) signals, which arise from the nonlinear susceptibility of a material. SHG signal is spectrally separable from autofluorescence in multiphoton microscopy and is commonly implemented as an additional color channel in commercial microscopes [59,60].

The goal of this paper is to devise and establish a neuroimaging tool that can capture the structure, metabolism, and biochemistry of the neuronal environment over large scales and do so dynamically on the same timescale as neuronal activities. The versatility of this tool is ensured by engineering a single optical source to extract all contrasts simultaneously, the microscale resolution and imaging speed of each contrast, and the computationally accelerated excitation or detection of each modality for real-time imaging. We present versatile autofluorescence lifetime, multiharmonic generation, polarization-sensitive interferometry, and Raman imaging in epi-detection (VAMPIRE) microscopy as a solution to this problem [Fig. 1(b)]. VAMPIRE microscopy utilizes three orders of light-matter interactions by evoking signals from the UV to the NIR from six processes simultaneously with a single laser, each accelerated using optoelectronic and computational techniques for fast imaging. Fast FLIM was implemented with computational photon counting on a field programmable gate array (FPGA) for 4× compressed sensing, followed by real-time processing on a graphical processing unit (GPU) (Note S2, Supplement 1). Polarization-sensitive OCM in the spectral domain was achieved using a single detector through polarization multiplexing, followed by real-time processing on a GPU. Multispectral CARS with femtosecond pulses was achieved using TOSS-CARS. Advances in supercontinuum generation on a photonic crystal fiber, amplitude and phase shaping on a Fourier transform pulse shaper, and effective utilization of the spectral windows were utilized to generate, optimize, and combine the excitation for each modality [Fig. 1(c)]. First, dual-channel fast FLIM with computational photon counting on an FPGA is demonstrated as an effective tool for imaging neuronal metabolic dynamics. Next, we highlight the utility of VAMPIRE microscopy to visualize the large-scale brain and retinal microenvironments rapidly. Third, the dynamic images of the *ex vivo* brain and the retina clearly show how the multidimensional information can be effectively utilized as a "functional contrast" for the components within the neuronal microenvironment, which would not have been possible without fast or simultaneous acquisition.

2. RESULTS

A. Metabolic Dynamics of Neurons in Response to Optical Stimulation Captured with FPGA-Accelerated Fast FLIM of NAD(P)H and FAD

We have previously shown that the photocurrent from a hybrid photodetector can be converted to photon counts with count rates of over 500% using a high-speed (GHz) digitizer, a hybrid photodetector (HPD), and the single-and-multi-photon peak event detection (SPEED) algorithm [61,62]. In this study, we expanded our fast FLIM setup to two channels and utilized the FPGA for compressed sensing (Fig. S2, Supplement 1). Since the photocurrents are not used further for FLIM processing anywhere in the pipeline, the compression can be considered lossless for its intended application (Figs. S3 and S4, Supplement 1).

The experiments in this sub-section establish the dual-channel fast FLIM of NAD(P)H and FAD as optimal tools for observing neuronal metabolism dynamics. The simultaneous measurement of fast FLIM of NAD(P)H and Ca^{2+} indicators is described in Figs. S5 and S6 and Note S3 in Supplement 1. Primary hippocampal neuronal cells transfected with CHETA-YFP [63] were imaged at 1.33 s per frame [Fig. 2(a)]. The sample was optically simulated with wide-field continuous-wave 470-nm light (<3 mW) for 3 s using a fiber-coupled LED. The NAD(P)H and FAD intensity responses were PCA-filtered; the first eight components were processed with a k-means clustering algorithm for each pixel [Fig. 2(b)]. A cluster size of four was chosen because the mean responses of no two clusters had a correlation coefficient of above 0.25, indicating no duplicates. The spatial arrangement of these clusters clearly encompasses different cells within the field of view (FOV), indicating a "functional contrast" between the cells from their label-free temporal autofluorescence dynamics. First, the pixels in cluster Sγ respond to the optical stimulation with an initial dip to the NAD(P)H intensity, followed by a rise (black arrow). A similar momentary dip is observed in their lifetime values for each stimulation. This suggests that there is a transition from NADH to NAD^+ and FAD to $FADH_2$ immediately after neuronal stimulation. However, the trends in all contrasts are reverted after $\sim 20-30$ s, which suggests alternative metabolic pathways for these cells. This is likely from cluster Sβ, which only responds to the first stimulation with an increase to the NAD(P)H and FAD intensity. The increase in intensity in the NAD(P)H channel in Sβ is not as much as the ones for cluster Sγ. The pixels in this cluster also have a continuous decrease in their fluorescence lifetimes following optical stimulation. This suggests a conversion from NADH to NAD^+ in the cytosol of these cells, which happens during pyruvate-to-lactate conversion. Astrocytes have been shown to fulfill this role in the neuronal environment previously. Similarly, the cluster Sα, which had higher initial NAD(P)H and FAD lifetime values, has the opposite trend in intensity to the cluster Sγ and has decreasing lifetime values following the optical

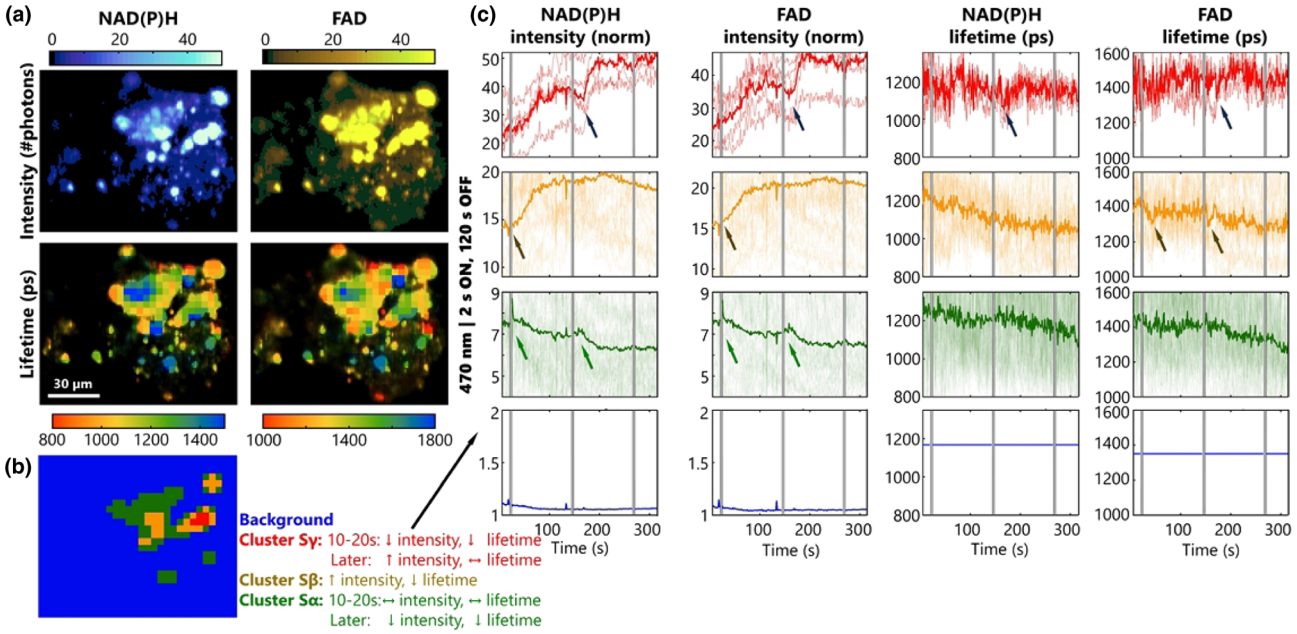

Fig. 2. NAD(P)H and FAD dynamics in response to optical stimulation of neurons. (a) Mean NAD(P)H and FAD intensity and lifetime images over a 320-s period. (b) Results from clustering the PCA-filtered NAD(P)H and FAD intensity dynamics for the image series in a following stimulation with 470-nm light 3 s on and 120 s apart. (c) Individual (transparent) and the average (solid and colored) FAD and NAD(P)H dynamics for each cluster in (b). The gray lines indicate the instances of optical stimulation when the detection shutter was turned off to prevent damage to the HPD.

stimulation. This suggests a conversion from bound NADH to NAD^+ and $FADH_2$ converted to FAD as the dominant processes within these clusters. These trends happen during processes such as pyruvate-to-lactate conversion and ROS (reactive oxygen species) scavenging, respectively. This suggests that these cells support the neuronal cells by performing alternative processes to ATP production to support the neuronal cells in cluster Sγ. Finally, there is an obvious background cluster with minimal changes to the NAD(P)H of FAD intensities and no discernable lifetime values due to the low insufficient photon counts. The response at higher stimulation frequencies is described in Note S4 and Fig. S7 (Supplement 1). The NAD(P)H and FAD dynamics of neurons in response to stimulation with glutamic acid are described in Note S5 and Fig. S8 (Supplement 1).

These results confirm previous observations such as the initial dip in NAD(P)H intensity following excitation or the glucose depletion in neurons following repeated stimulation [5]. While dual-channel fast FLIM was an optimal tool to image the redox and metabolic dynamics associated with electrical activity, the two modalities are not sufficient for holistic characterization of the neuronal environment. The next sections explore the combination of fast FLIM with OCM and CARS in VAMPIRE microscopy for imaging of neural tissues.

B. Changes to Scattering and Autofluorescence in the *Ex Vivo* Retina from Optical Stimulation

Figure 3 shows the mosaic and axial stack of different fields of view in an isolated retina and with the various contrasts of VAMPIRE microscopy. Freshly extracted retinae from a 3-month-old albino mouse following euthanasia by CO_2 asphyxiation were placed in imaging dishes with freshly prepared and pH balanced Ames' medium within a stage top incubator mimicking physiological conditions. The retinal ganglion cells (RGCs) are abundant in the inner layer beneath the vitreous humor and the limiting membrane 10–20 μm below the surface [Fig. 3(a)]. Due to the compartmentalization of metabolism in neuronal cells, the interface of the nerve fiber layer (NFL) and the RGC layer, which contains the highest density of axonal projections from the RGCs, is expected to have the brightest signals in the autofluorescence channels, and be the most informative for RGC metabolism under our microscope [Fig. 3(c)]. From the axial stack shown in Fig. 3(b), the depths between 10 and 30 μm show both neuronal fibers and cell bodies, suggesting an interface between the retinal ganglion cells and the nerve fibers. The fiber tracts are also apparent in the lifetime images, with a typical lifetime of 1200 ps, compared to the background where the variation was higher. Nonetheless, the dynamics presented in the section further were acquired at a depth of 10–20 μm, which had the best structural contrasts and signal-to-noise ratio. Figure S9 in Supplement 1 is the multimodal image of a retina *ex vivo* acquired using VAMPIRE microscopy averaged over the duration of imaging for dynamics. The cells are highlighted with white arrows. While most of the RGCs help in processing the visual information detected in the photoreceptor layer, a subset of RGCs is intrinsically photosensitive and is expected to respond to optical stimulation immediately. The presence of these neurons also induces birefringence from the presence of neuronal fibers. Figure S10 (Supplement 1) shows the percentage change to each contrast and the intercept for 50 s following each excitation. The shifts are not monotonically increasing or decreasing for the entire FOV, negating the presence of any global trends. Within local populations, the trends are consistent for every excitation pulse.

The response to optical stimulation was analyzed by extracting the average slope and intercept for 25 samples following the excitation pulse for each super pixel [Fig. 4(a)]. The mean trends indicate that, despite changes to the fluorescence intensities in both the NAD(P)H and FAD channels, the changes to the overall fluorescence lifetimes, especially in the FAD channel, are minimal.

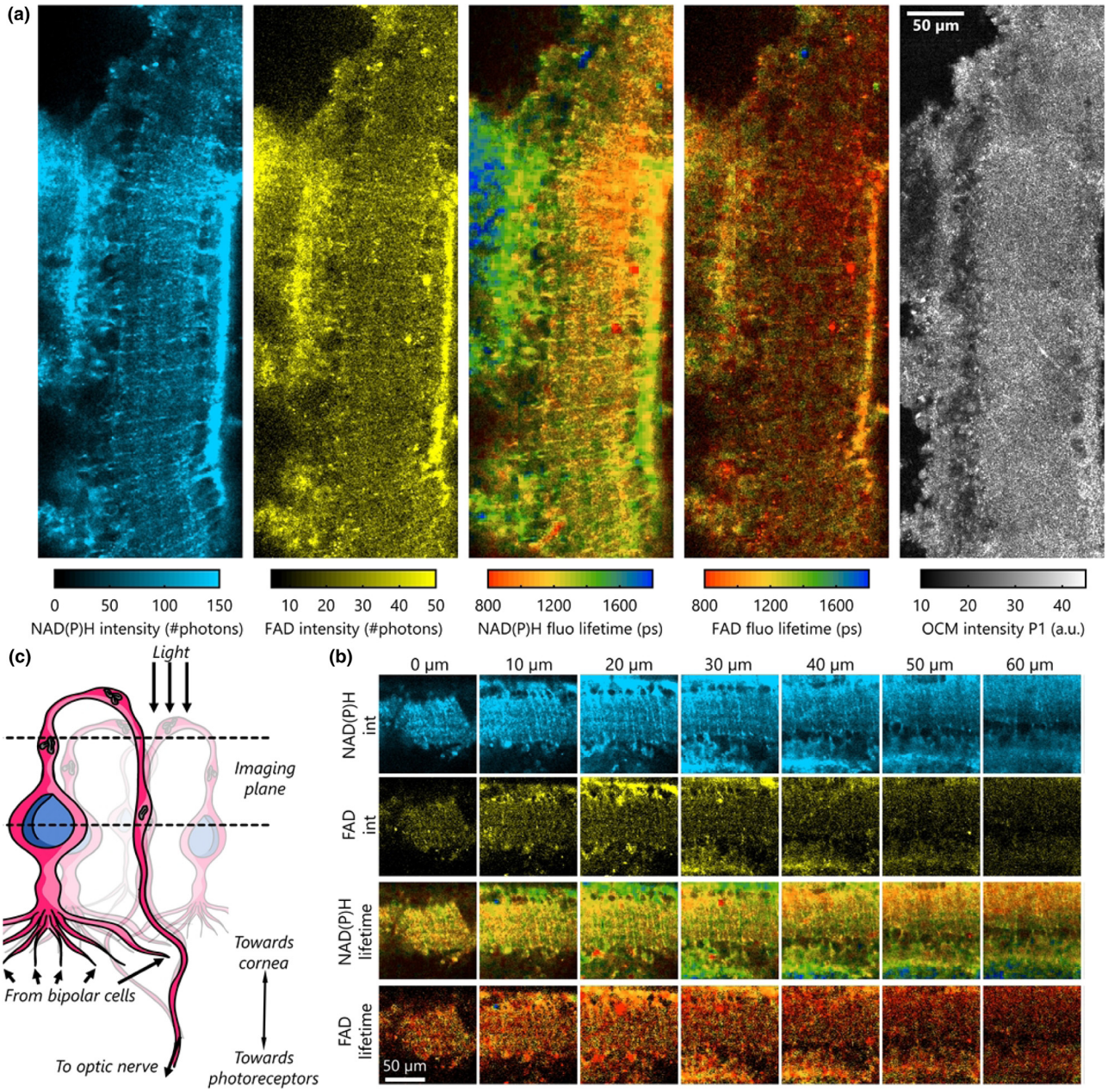

Fig. 3. (a) Mosaic and (b) *z*-stack of a mouse retina imaged *ex vivo* between the nerve fiber layer and the ganglion cell layer. (c) Cartoon showing the orientation of the retinal ganglion cells in the retina and the imaging plane for the results in Fig. 4.

Visually, some of the slopes in the OCM channel appear to be similar to the changes in intensities. The slopes normalized to the intercepts were used as inputs to the clustering algorithm. Cluster 1 (green) represents background responses, with minimal changes to optical activation, except for some subtle changes to the FAD intensity. Cluster 2 (yellow) represents responses from cells with an immediate decrease in the NAD(P)H and FAD intensities following optical activation, followed by recovery to the original intensity values. Interestingly, the responses in the FAD channel are repeatable for every optical activation, whereas the responses in the NAD(P)H channel progressively decrease in magnitude for every excitation pulse. A similar trend is observed in the OCM intensity channel, which only shows a response for the first excitation pulse. Clusters 3 (pink) and 4 (red) are from regions that show an immediate increase in the fluorescence intensities of NAD(P)H and FAD following each excitation and recovery to lower intensities. The NAD(P)H intensities are expected to return to baseline values in 218 s and 185 s, for clusters 3 and 4, respectively, and 267 and 140 s for clusters 3 and 4, respectively, for the FAD intensities. Interestingly, the OCM intensities in both polarization states also show responses to optical stimulation in response to each excitation pulse. This also suggests a change to the overall cellular morphology in these regions. The different fall times in the intensities also suggest different metabolic states for these cells following neuronal activations. Figure 4(c) also shows the various clusters highlighted in the different modalities. First, cluster 3, in which both the autofluorescence intensity and OCM intensity respond

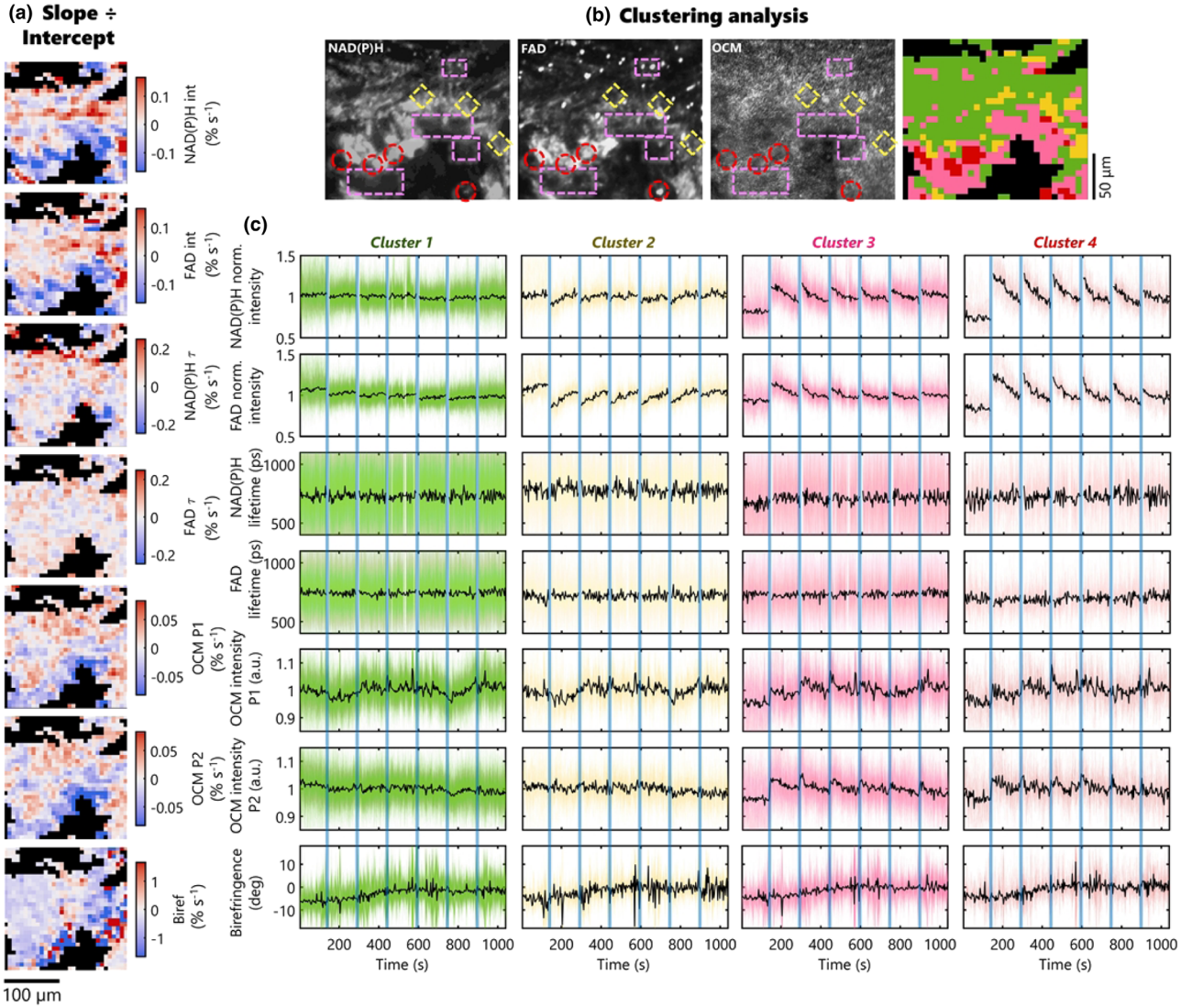

Fig. 4. Optical stimulation of retina *ex vivo* imaged with VAMPIRE microscopy. (a) Average normalized slopes. (b) *k*-means clustering results based on the slopes and intercepts, and the interpretation in each modality. The regions that are prominent under cluster 2 (yellow) are highlighted as rhombuses, cluster 3 (pink) are highlighted as rectangles, and cluster 4 (red) as circles. (c) The individual (transparent and colored) and median (black and solid) trends of each contrast for each cluster are shown at the bottom.

to the optical excitation, appears to contain the ganglion cells with a visible nucleus within the FOV. While cluster 4 has a similar temporal response to cluster 3, it is made of sub-cellular (5-µm large) structures with bright autofluorescence in both NAD(P)H and FAD channels. Interestingly, cluster 2 appears similar to cluster 3 structurally in the FAD channels as ganglion cells with a bright nucleus. This highlights how imaging with VAMPIRE microscopy can discern functional contrasts between neuronal subtypes. It is important to note that when the clustering algorithm was run on each individual channel, the "functional contrast" was not as informative as utilizing the multimodal data (Fig. S11, Supplement 1). The retina did not have sufficient CARS signals at the imaging speeds. However, the neuronal microenvironment of the brain is denser and has more lipids. The brain is also more scattering than the retina, causing higher CARS signals in the epi direction. This enables rapid characterization of the diversity within the neuronal microenvironment of the cortex in the mouse brain presented in the next section.

C. Multimodal Signature of the Mouse Brain Microenvironment Imaged with VAMPIRE Microscopy

Figure 5(a) shows the various combinations of overlays of the contrasts obtained using VAMPIRE microscopy as a 36-panel mosaic. Two regions are highlighted within this large area. Figure 5(b) highlights a blood vessel in the field. The blood vessel content is less scattering than the surrounding neuronal fibers in the OCM channel and has minimal CARS signals. However, the individual blood cells are apparent in the NAD(P)H and FAD channels. The dense neuronal fibers are highlighted in Fig. 5(c). OCM can capture the micron-scale neuronal fibers within bundles; these regions also have high birefringence compared to surrounding areas. While some of these fibers are visible in the NAD(P)H channels, a majority of the autofluorescence is localized to a few regions within these tissues, which also coincides with the strong signals from the CARS channels. This further reiterates the compartmentalized metabolism of neuronal tissues. The speed and multidimensional information available through VAMPIRE microscopy provide

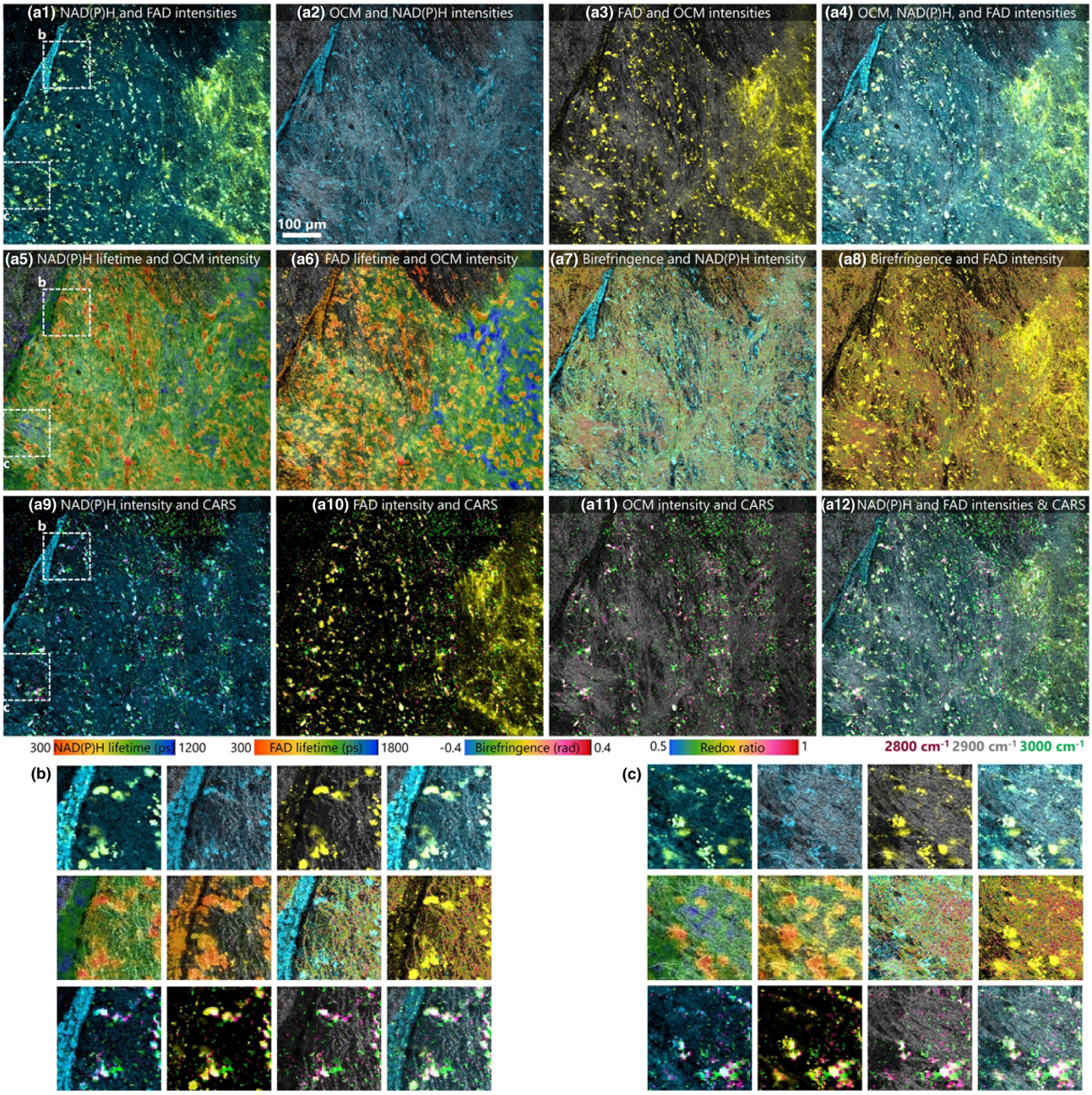

Fig. 5. Images of a mouse brain slice near the cortex using the VAMPIRE microscope. (a) 6 × 6 mosaic spanning 700 × 700 μm with two regions zoomed in highlighting a (b) blood vessel and (c) neuronal fibers. Each panel in the mosaic shown here is a 24-frame average (eight frames for each spectral window in CARS).

immense and unique insights into the neuronal microenvironment. Visualization 1 of the brain is also highlighted in Movie S1 and Figs. S12–S14 in Supplement 1.

Next, the dynamics of the brain within the cortex region were explored. The neuronal microenvironment of the brain differs drastically from that of the retina, especially apparent in the OCM channels. The images in Fig. S15a (Supplement 1) were acquired in the cortex region from brain slices. More neuronal fibers and bundles are apparent within the FOV. A few cell bodies are apparent in the NAD(P)H and FAD channels. The range of birefringence was also larger than that of the retina, due to the ordered and denser alignment of the neuronal fibers. Several lipid particles are apparent in the CARS channel (as bright green dots), which coincide with bright spots either in the NAD(P)H or the FAD channels. They also have lower fluorescence lifetimes compared to the rest, typical of lipids. The change to the slope in the brain appears to be less than that in the retina (Fig. S15b, Supplement 1). Nonetheless, the shifts are not monotonically increasing or decreasing for the entire FOV, negating the presence of any global trends. The intercepts are also fairly consistent across the entire time scale (Fig. S15c, Supplement 1). This demonstrates the noninvasive nature of VAMPIRE microscopy and its capability to observe the dynamics of neurons over 1000 s. The average slopes normalized to the intercepts are shown in Fig. 6(a).

Five distinct populations were observed in the clustering analysis [Figs. 6(b) and 6(c)]. Clusters 1 and 3 had minimal changes

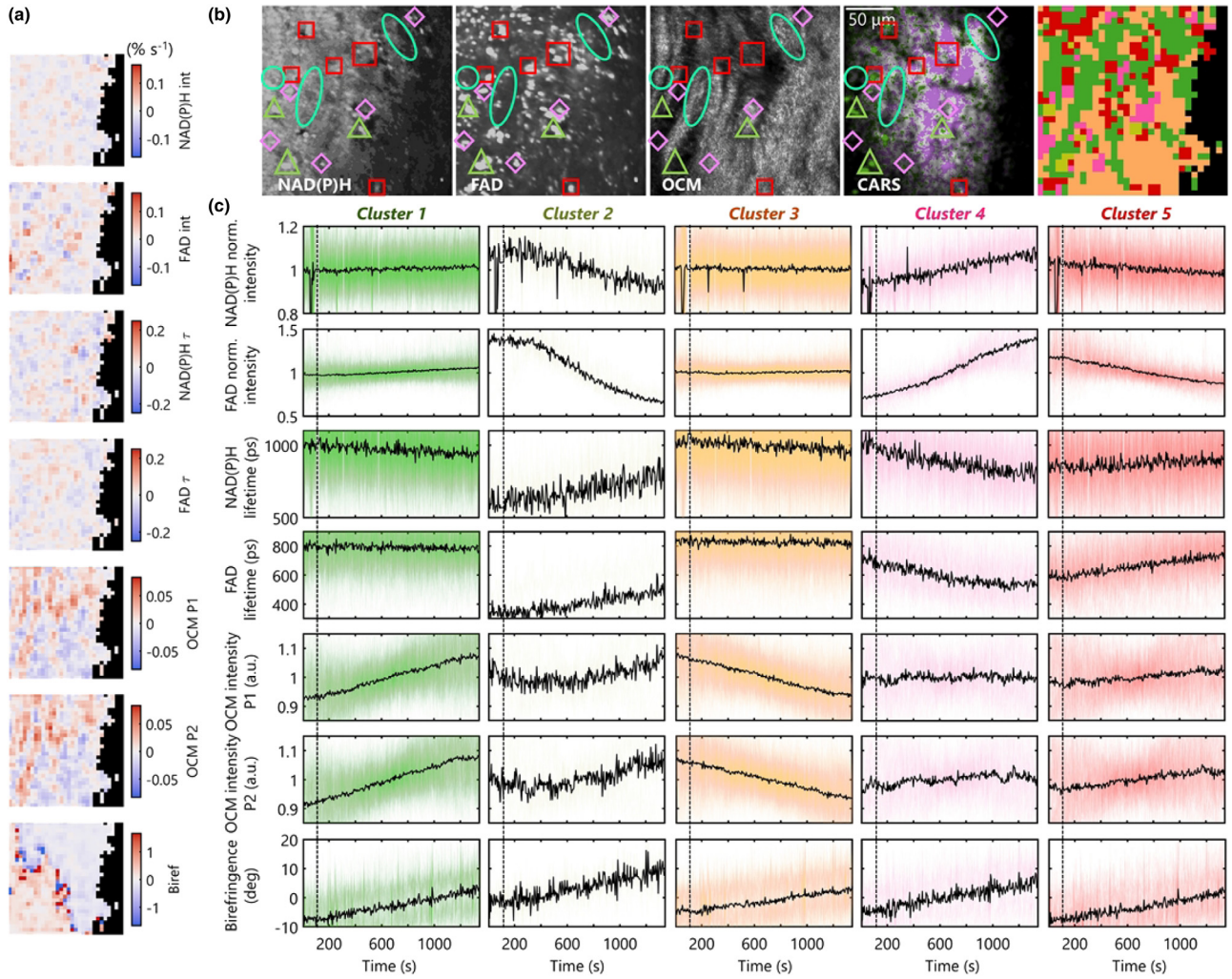

Fig. 6. Fast imaging of neuronal activity in the brain using VAMPIRE microscopy. (a) Average normalized slopes. (b) *k*-means clustering results based on the slopes and intercepts, and the interpretation in each modality. The regions prominent under cluster 1 (cyan) are highlighted as circles, cluster 2 (green) as triangles, cluster 4 (pink) as rhombuses, and cluster 5 (red) as rectangles. (c) Individual (transparent and colored) and median (black and solid) trends of each contrast for each cluster in (c).

throughout the fluorescence lifetime channels, although they had opposing trends in the OCM intensity channel. However, this does not appear to be a response to the addition of glutamate; rather, it is an effect of continuous imaging due to tissue relaxation. The average fluorescence lifetime of both clusters is also higher than the other clusters. Clusters 2, 4, and 5 are initially silent and respond after the addition of glutamate in both fluorescent intensities. The response of cluster 2, a decrease in the fluorescence intensities of FAD and NAD(P)H, is particularly delayed by over 200 s, suggesting a delayed onset of the effect of glutamic acid addition. In contrast, both clusters 4 and 5 respond to glutamate stimulation within 20 s. There is also an overall change to the fluorescent lifetime values. The most prominent changes are apparent in the FAD intensity and OCM intensities, which are also apparent in the slopes [Fig. 6(a)]. The molecular origins of these changes were also investigated with CARS imaging. The CARS images were acquired for five different spectral sub-bands of the Stokes beam to generate CARS signals at 2830 cm^{-1}, 2930 cm^{-1}, 3030 cm^{-1}, 2800 − 3100 cm^{-1}, and block (generated by creating destructive interference of all wavelength components in the 1045-nm supercontinuum using the pulse shaper). Since the individual responses in each frame were weak, the signals were analyzed across four larger time bins. First, TOSS-HS-CARS in VAMPIRE microscopy could image the brain biochemistry label free over long durations (Fig. S16, Supplement 1). Second, the three different vibrational bands captured highlight different parts of the sample (Fig. S16a, Supplement 1). Third, with ratiometric analysis, there is an increased occurrence of pixels with very low or very high lipid-to-protein ratios (Figs. S16c, S16e, Supplement 1). Visually, there appears to be an increase in the number of "green" dots in Fig. S16d (Supplement 1) over time, suggesting an increase in lipid production over this process.

The relationship between the time-series imaging, clustering analysis, and the sample structures is presented in Fig. 6(c). The cyan cluster (cluster 1) is prominent along a subset of the neuronal fibers apparent in the OCM channel. In the CARS images, these regions neither have a dominant protein peak nor a lipid peak. These regions do not have strong autofluorescence either, suggesting that these correspond to bundles of nerve fibers. Therefore, the changes observed in the OCM channels in these regions could be attributed to subtle shifts in the focal plane, where the scattering of the fiber bundles could be different within a small axial range due

to the thin aligned structures. While clusters 2, 4, and 5 responded to glutamate stimulation, they have different biochemical and metabolic properties. For instance, cluster 2 (green triangles) contains strong lipid peaks observed in the CARS channel, which also have strong NAD(P)H and FAD fluorescence. While clusters 4 and 5 appear alike in the OCM and autofluorescence channels, cluster 5 (red squares) has more lipid content than cluster 4 in the CARS channel, though weaker than cluster 2. Tracking these regions in the CARS channel across time in Fig. S16 (Supplement 1), it is apparent that these lipid particles appear only in the later frames, suggesting synthesis in response to neural activity. The results, when the resolution was prioritized over the imaging speed, are presented in Note S6 and Figs. S17–S19 (Supplement 1).

3. DISCUSSION

The incredibly complicated processes behind neuronal metabolism arise from their high energy demand, diverse cellular functions, specialized morphology, adaptation, and glial interactions. Additionally, their dynamics are often subdued by the inherent redox balance and neuroprotection. Neurons are highly vulnerable to oxidative stress due to their high oxygen consumption, abundant membrane lipids, and limited regenerative capacity [64]. Maintaining redox balance and antioxidant defense mechanisms involves complex metabolic pathways to protect neurons from oxidative damage and maintain cellular viability [65]. Additionally, neurons communicate with each other through synapses, where neurotransmitters are released and received [4]. Synaptic transmission involves the reuptake, recycling, and synthesis of neurotransmitters, which require energy and metabolic resources. The regulation of neurotransmitter metabolism and availability adds to the intricacy of neuronal metabolism. The experiments in this paper only serve to establish the dual-channel fast FLIM of NAD(P)H and FAD as optimal tools for observing the dynamics of neuronal metabolism. These results confirm previous observations of the initial dip in NAD(P)H intensity following excitation or the glucose depletion in neurons following repeated stimulation [5]. A detailed understanding of neuronal metabolism often requires measuring metabolite levels, enzyme activities, and metabolic fluxes using complementary techniques such as metabolomics or enzymatic assays [16]. Recent studies have shown that FLIM could quantify the metabolite concentrations [66]. Furthermore, in this paper, the NADPH dynamics were assumed to be minimal compared to the NADH dynamics in response to neuronal activity. However, NADPH has been shown to play a key role in neuronal nitric oxide synthase for communication and plasticity [67], the neuronal antioxidant system [68], and neuronal detoxification [69].

The metabolism of the RGCs is remarkably complex, where each cellular compartment could have different responses to activation. The retina is also one of the most oxidative tissues in the body, especially the inner retinal layers [70]. It is important to note that most of the neurons in the retina are inhibitory. Also, intrinsically photosensitive RGCs are, in fact, a minority, both in numbers and their excitatory nature. The RCGs span several retinal layers, starting from their dendritic projections within the inner plexiform layer, the soma in the ganglion cell layer, and the unmyelinated axons projecting onto the nerve fiber layer (innermost layer) initially, after which the myelinated parts of the axon join the optic nerve back into the outer retinal layers [71] [Fig. 3(b)]. The results in Fig. 4 were at the transition between the RGC soma and the unmyelinated axons. The unmyelinated axons have been shown to have varicosities rich in mitochondria [72], which supports their unusually high energy demands. The NFL also contains elevated levels of cytochrome *c* oxidase and Na^+ K^+ ATPase [73]. The former is a critical component of the electron transport chain. The elevated levels of the latter indicate an abundant degree of depolarizing and repolarizing activities. For the dynamics observed in Fig. 4, there were minimal changes to the fluorescence lifetime in response to optical activation. Therefore, based on Fig. S1 (Supplement 1), clusters 3 and 4, where the NAD(P)H and FAD intensities gradually decrease, are indicative of increased ETC. This is also apparent in the bright regions (in the autofluorescence channel) co-occurrent with the nerve fibers seen in the OCM (cluster 4). These could indicate the cytochrome-rich regions in the RGC axons responding to the increased energy demands from neuronal activation. It is also interesting to note that this phenomenon is only apparent in a small subset of cells and nerve fibers in this layer. The responses of over 50% of the pixels in this region are not synchronized to the optical stimulation. As a validation, a retina was imaged at the layer consisting only of RGC soma (Fig. S20, Supplement 1). The cell bodies are apparent in the fluorescence channels. Also, the neuronal fibers seen in the previous region in the OCM channel are absent here. None of the clusters appears to have any dominating response to photoactivation in this FOV, further highlighting the compartmentalization of the retinal metabolic responses.

Due to the diversity among the retinal ganglion cells, the molecular composition of the various cell types inferred from the functional contrast could not be tagged with one or two markers for validation. One avenue for this could be using advances in spatial genomics after fixation to get the molecular profiles of these cells [74]. While matching the FOV in sectioning will be challenging, marking the adjacent regions with ablation could help with this registration. For brain imaging, while the 770-nm excitation does not excite popular fluorophores with emission in the green-to-red spectral regions, the Stokes beam will excite these wavelengths near their peak and their emission will overlap with NAD(P)H and FAD spectra. Therefore, future studies could sacrifice CARS imaging to validate the neuronal cell subtypes in the brain to their functional responses. In brain imaging, the autofluorescence changes were most prominent in lipid-rich regions in the tissue. In this case, the interpretation of the autofluorescence trends is complicated by the lipid autofluorescence that could be present in both NAD(P)H and FAD channels. Cluster 5 was not from the lipid-rich regions but showed a decrease in the FAD and NAD(P)H intensities and an increase in the FAD lifetime in response to glutamate stimulation. Together, from Fig. S1 (Supplement 1), one could infer this as an increase in the ETC process within these cells. However, since glutamate stimulation also causes oxidative stress in the tissue, the changes to the NAD(P)H fluorescence could be from NADPH dynamics as a ROS scavenger. These trends would be difficult to interpret from the responses of any single imaging modality of VAMPIRE microscopy.

A constant argument against simultaneous multimodal imaging is sacrificing the synchronized acquisition and speed for the sake of simplicity in system design. In this paper, we have clearly established the utility of simultaneous, synchronized, and fast multimodal acquisition. The analysis that was performed in Figs. 4 and 6 was rerun considering the slopes and intercepts of a single contrast at a time and shown in Figs. S11 and S21 (Supplement 1).

The dynamics in the retina during optical stimulation were more pronounced than that in the brain for each contrast. Therefore, the clustering when each contrast is considered has some visual similarities to the results from when all contrasts are considered. This is particularly highlighted when the NAD(P)H, FAD, and OCM intensity trends are considered. However, each of these results is harder to interpret and noisier than the clustering for all contrasts. In the brain imaging results, this disparity between considering all contrasts and one at a time is larger. Apart from the FAD intensity channel, interpreting the clustering results to the structure is difficult. The combination of these modalities, along with the clustering analysis, not only serves as a method to get functional contrasts between the different components of the tissue but also helps interpret the metabolic trends more accurately with the structural and biomedical contexts. The speed and non-invasive nature enabled long-term fast imaging of neuronal tissues in their physiological conditions label free and rapid characterization of neuronal tissues over a larger FOV with sub-micron resolution completely label free with a single tool. In this multimodal system, the cost is dominated by the femtosecond tunable dual-output laser. As an added advantage, the single source excitation, enabled by recent advancements in supercontinuum generation and pulse shaping, aids in synchronization and avoids the costs for additional sources for the other modalities.

An ideal neurophysiology tool would be able to directly measure electrical activity (as currents or potentials). However, the label-free contrasts are not specific to just the changes to the electrical activity. For instance, optical phase changes can be induced by any phenomenon that causes a change to the cell shape, density, volume, or refractive index. Even for action potentials, while the sodium ion flux is prominent for the first few milliseconds, the Ca^{2+} ion flux could last several seconds. Decoupling one effect from the other needs additional information or simpler biological models. Similarly, cellular motion will cause reorientation of the cytoskeletal structures, and, consequently, changes to the birefringence. The autofluorescence characteristics are not only affected by changes to the metabolic states of the cells and tissues, but also by the changes experienced by NADPH or other flavoproteins that respond to the changes to the microenvironment unrelated to metabolism such as pH changes or neurotransmitter release, or other autofluorophores not considered in the model, such as lipids and LipDH. Additionally, the timescales of measurements are also different for these modalities. Therefore, rather than concentrating on being able to extract the cellular potentials, this paper has concentrated on exploring the changes in the label-free contrasts because of neuronal activity. For the OCM setup in the VAMPIRE microscope, the phase stability of each polarization state was low due to the long optical paths. However, because of polarization multiplexing, the overall phase difference between the two states was stable across time with a standard deviation of <5 nm.

The autofluorescence from neurons and neuronal tissues is weaker than other cell types. For instance, the average intensity (in measured photon counts) in the NAD(P)H channel per single laser pulse at the same power was 0.42 for a sample of a mouse kidney, 0.81 for a sample of a rat tail, 0.33 for a sample of a mouse heart, and <0.02 for mouse brain and retina. Similarly, for cancer cells (MDA-MB-231 cell line) imaged with the same setup, the average photon count ranged from 0.3 to 2.00 (up to 3.00) per laser pulse [61,62], whereas, for the neuronal cells, it was between 0.015 and 0.05. This $20\times$ reduction in the autofluorescence intensity demands higher exposure times (more laser pulses incident per pixel). Neurons are highly metabolically active and possess efficient mitochondrial functions [75]. Neuronal mitochondria exhibit efficient electron transport and lower levels of oxidative stress, resulting in reduced autofluorescence from mitochondrial fluorophores. Additionally, neuronal tissue has a relatively low concentration of endogenous fluorophores compared to other tissues [76,77]. The lower concentration of these fluorophores in neurons results in reduced autofluorescence signals. The lower autofluorescence intensity also creates issues in the estimation of fluorescence lifetime values [78]; more photons have to be considered to accurately estimate the fluorescence lifetime. Therefore, the imaging speed in this paper was between 0.05 and 1 Hz. This is slow even for Ca^{2+} dynamics, although fast enough to capture previously reported metabolic changes from neuronal activity. While computational photon counting with SPEED for FLIM improved the overall dynamic range of acceptable photon counts and the imaging speeds, the fundamental limitation was the low autofluorescence within the sample itself. In this study, the shortest pulse width at the sample plane with the multiphoton laser was 170 fs. With better laser sources, this could be further compressed to sub 100 fs for a $2-4\times$ improvement in the signal levels.

CARS microscopy of neurons had a similar limitation as autofluorescence. The signal levels were estimated to be between 0.05 and 0.2 photons per laser pulse, of which a non-negligible portion is from the non-resonant background. Additionally, in the prototype TOSS-HS-CARS setup in this paper, the maximum power at the sample plane in each sub-band of the Stokes beam was less than 3 mW. In this paper, the photonic crystal fiber (PCF) was pumped at 60% of the maximum output of the laser because pumping it at higher powers caused back reflections that caused instabilities with the laser cavity. With better laser design and isolation, this power could be increased further. Improving the efficiency of supercontinuum generation and the pulse shaper could help improve the signal levels of CARS and enable faster imaging. Additionally, for hyperspectral data, the Stokes pulses were varied between four to six patterns, thereby restricting the effective speed of HS-CARS to be less than the other modalities. CARS microscopy was used to characterize the dynamics in the samples in this paper. Raman scattering microscopy in the neurosciences is more prevalent for studying the pathways behind neurodegeneration, neuroinflammation, and injuries, which will be the focus of future studies [79].

The weaker signals from these samples necessitated cumulating responses from several individual pixels into super pixels. While the structural imaging yielded images with diffraction-limited resolution in each modality, the effective resolution of dynamic imaging was reduced. For the same image dimensions, the effective resolution could be improved by scanning a smaller field of view. The fields of view in this paper were chosen to ensure minimal photodamage during dynamic imaging such that the illumination is not persistent at any single location in the sample at the specified optical powers. The tradeoff between the field of view (and, consequently, the effective resolution) and the optical powers could be tuned based on the application. For instance, for more scattering samples or samples with higher CARS signals, the Stokes and OCM powers could be reduced with a corresponding increase in the pump power for stronger autofluorescence.

While the SHG channel was available for detection in the current setup and was previously used to characterize collagen in previous versions of the microscope [80], the SHG signals in the

samples presented in this paper were negligible. However, SHG has previously been used for imaging action potentials in single neurons with labeling [81]. Matrix proteins like collagen and elastin play important roles in the development and activation of the nervous system [82]; future studies will utilize the SHG in VAMPIRE microscopy to study these aspects.

The FPGA-accelerated compressed sensing and GPU-accelerated processing were critical to maintaining fast imaging speeds for long durations. The raw data throughput of VAMPIRE is 20 GB/s for fast FLIM, 160 MB/s for PSOCM, and 320 kB/s for CARS and SHG. Each 256 × 256-pixel frame at 1024 laser pulses per pixel was compressed at 16.78 GB down to 4.19 GB after processing on the FPGA for NAD(P)H and FAD FLIM, 134.22 MB for PS-OCM, and 262.144 kB for SHG and CARS (4.32 GB total). For sustained imaging, the overall frame rate had to be less than 0.35 Hz (42% of the maximum frame rate based on the exposure time per pixel and total number of pixels). If the data throughput could be improved, along with the improvements to the signals discussed in the previous section, faster dynamics could be explored in the future. This also provides an opportunity for future studies for a further degree of compression (to 2 bits) if one does not expect more than three simultaneously arriving photons for another 2× reduction to the data stream. PCIe speeds of 4–6 GB/s can be sustained in the absence of any background processes. However, with the data acquisition software used and the other components such as the data acquisition (DAQ) card and the GPU, the effective PCIe transfer speeds for over 2 min of continuous streaming were measured to be 3.2 GB/s. The 2× reduction to the data stream will help accelerate image acquisition further.

To our knowledge, this is the first implementation of optical multimodal imaging with the combination of extracting the polarization, scattering, autofluorescence lifetime, and coherent Raman scattering at multiple vibrational energy levels. The combination of two-photon FLIM with multispectral CARS simultaneously has been a long-standing challenge at higher frame rates since existing methods either need longer exposure times if one were to use femtosecond pulses with spectrometer-based CARS detection or weaker signals if one were to use picosecond pulses for spectral-focusing CARS. The techniques in VAMPIRE overcame this issue. Previous optical multimodal platforms could do a subset of these contrasts, sometimes simultaneously. A table comparing VAMPIRE microscopy to previous studies is summarized in Table S1 and discussed in Note S7, Supplement 1 [28,83–89].

This paper sought out to explore the utility of label-free multimodal optical microscopy for imaging neuronal structure and activity. Several label-free contrasts, previously used to study neural activity, were made faster, combined for co-registered multimodality correlations, and optimized for imaging neuronal samples across a large spatiotemporal scale. Although quantitative electrophysiology with label-free imaging needs further work, the techniques presented in this paper could observe spontaneous activity, responses to chemical stimulation and suppression, and responses to optical excitation. This is a key step in the paradigm shift from low-throughput electrophysiology to high-throughput optophysiology for fundamental neuroscience and clinical applications. For instance, Alzheimer's disease (AD) is a neurodegenerative disorder known to progressively cause memory deficits and broader cognitive impairment as the disease progresses. Post-mortem, AD is verified by the presence of hyperphosphorylated tau in neurofibrillary tangles and amyloid beta (Aβ) plaques, detected by immunohistochemical staining of the brain tissue. It is commonly believed that, collectively, the accumulation of these in the brain impairs neuronal function and communication, which eventually manifests into severe dementia as patients age. Label-free optical imaging presents a unique and convenient means for identifying these biomarkers, tracking disease progression, and determining disease severity.

As a research system, the optical platform presented here can be used for other applications, including cancer biology and for biofilm imaging, since these label-free contrasts are ubiquitous among biological samples. Additionally, we had demonstrated the utility of adaptive optics in a similar multimodal system [89], which can be adapted to VAMPIRE microscopy. This, combined with the epi detection, also enables *in vivo* imaging experiments with minimum modifications. While the individual modalities are prevalent in clinical imaging, this paper highlights the advantages of combining these modalities, with minimal additional cost for the laser sources. The complexity in the optical design and processing could be optimized based on application and making the components more modular. While these additional advantages are beyond the scope of the current study, they will be explored in the future.

4. MATERIALS AND METHODS

A. Optical and Electronic System Setup

Excitation and emission for FLIM. We employ a titanium-sapphire laser (Insight X3+, Spectra Physics) as the excitation source for our multiphoton imaging system. The titanium-sapphire laser (Insight X3+, Spectra-Physics) was operated at a central wavelength of 770 nm and 80 MHz. The shortest pulse width at the sample plane was measured to be 170 fs. A 605-nm dichroic mirror (FF605-Di01, Semrock Inc.) was used to separate the excitation and emission light, and a 505-nm dichroic mirror (DMLP505R, Semrock Inc.) was used to separate the NAD(P)H fluorescence from FAD or Calbryte 590 AM fluorescence. A pair of 633-nm short pass filters is placed in the detection path before the 505-nm dichroic to prevent any excitation light leaking into the detector. When imaging Calbryte 590 AM fluorescence, a 665-nm dichroic mirror (FF665-Di01, Semrock Inc.) and a 585-nm long pass filter were used in the Calbryte 590AM detection path and a 450 ± 70-nm filter was placed in the NAD(P)H detection path. This path can be discerned by following the pink, yellow, and blue paths in Fig. 7. The SHG signal was detected using an analog PMT (H10721-210, Hamamatsu), amplified by a transimpedance amplifier (TIA-60, Thorlabs Inc.).

Excitation and interferometry for OCM. A part of the 770-nm beam is used to pump a PCF (LMA-PM-5, NKT Photonics) for an output power of 300 mW and a bandwidth of 120 nm (base-to-base). The output of the PCF is collimated with a parabolic mirror for an initial beam diameter of 12 mm and linearly polarized with a linear polarizer. This beam is directed into the interferometer directly after passing through a quarter-wave plate and 0.2× magnification. The OCM beam is combined with the Stokes and pump beams using a cube beam splitter. Polarization-sensitive OCM was enabled using polarization delay multiplexing in the reference arm. This can be discerned by following the gray path in

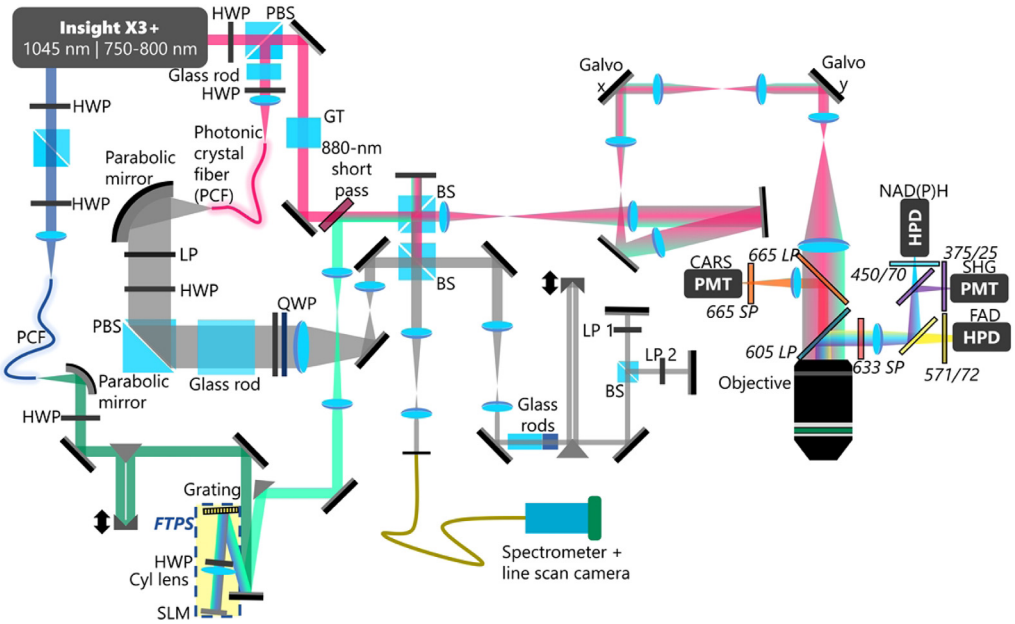

Fig. 7. System setup for VAMPIRE microscopy. HWP: half-wave plate, PBS: polarizing beam splitter, GT: Glan-Thompson polarizer, SLM: spatial light modulator, BS: beam splitter cube, LP 1,2: linear polarizer, Galvo: galvanometer scanning mirror, PMT: photomultiplier tube, HPD: hybrid photodetector, # SP/LP: short pass/long pass filter with cutoff at # nm.

Fig. 7. The combined OCM beam underfilled the back aperture of the objective lens by design for higher depth of field.

Excitation and emission for CARS. The differences between spectral focusing CARS and TOSS CARS, and the advantages of the latter, are discussed in detail in Yang *et al.* [33]. A brief description is summarized in Note S8 (Figs. S22–S24) in Supplement 1. A supercontinuum spanning 200 nm base-to-base was generated by 1.3 W of 1045-nm output coupled into a photonic-crystal fiber (PCF, LMA-PM-10, NKT Photonics). The custom FTPS (Fourier transform pulse shaper) consists of a diffraction grating, an achromatic half-wave plate, a cylindrical lens, and a 2D spatial light modulator (SLM). The shaped Stokes beam was coupled into the pump path using a dichroic mirror after matching both polarizations using a half-wave plate. The collimation of the Stokes beam was adjusted to ensure that the focal spot of the two beams was at the same plane in the sample. An optical delay line (ODL) was inserted between the PCF and the FTPS to delay the shaped Stokes beam by one laser pulse period (12.5 ns for 80 MHz) compared to the pump. We matched the path lengths by maximizing the sum-frequency-generated response from the interaction of the pump and the Stokes beam for a BBO crystal placed at the sample plane. The CARS emission was separated by a 665-nm dichroic. A 665-nm short pass filter (633SP, Semrock Inc.) is placed in the detection path for CARS and a 612/69-nm filter was used before the detector. This can be discerned by following the cyan and orange paths in Fig. 7.

Scanning and detection. The beam is scanned by a pair of galvanometer mirrors (6220H, Cambridge Technology) and focused through a 25× objective lens (Olympus Inc.). The fluorescence photons were detected using a pair of hybrid photodetectors (R10467U-40, Hamamatsu Inc.) that had a sub-500-ps rise and fall time. The photocurrents were amplified using a transimpedance amplifier (TIA, HSA-X-2-20, Femto). The OCM interferogram was captured using a fiber-based spectrometer (Cobra S 800, Wasatch Photonics) and one of two-line scan cameras (OctoPlus, Teledyne e2v; or Sprint spL4096-140 km, Basler Inc.). The CARS signal was detected using an analog PMT (H16722P-40, Hamamatsu), amplified by a transimpedance amplifier (TIA-60, Thorlabs Inc.).

The output photovoltages were measured with a 5-GHz two-channel digitizer (ADQ7WB, Teledyne SP Devices) purchased with the additional development kit offering access to the onboard FPGA. The FPGA was programmed with Vivado 11 (Xilinx). A PCIe-based DAQ card (NI 6353, National Instruments) was used to generate the clocks, triggers, and the analog waveforms to control beam scanning. The same DAQ was used to capture the SHG and CARS signals through analog inputs. Both the digitizer and the DAQ card were synchronized to the laser using a 10-MHz reference clock derived from the internal photodiode of the laser passed through a clock divider (PRL-260BNT, Pulse Research Lab) and a fanout buffer (PRL414B, Pulse Research Lab). Since 5 GHz is not divisible by 80 MHz, there are 125 samples collected per two laser periods and are processed together for phasor analysis for two cycles of the laser period. The OCM camera was connected to a PCIe-based frame grabber (NI 1433, National Instruments) and synchronized with the DAQ card for each line scan. This is summarized in Fig. S25 (Supplement 1). The transverse resolutions of the fluorescence channels were 0.4 and 1.2 μm for CARS, limited by the NA of the objective lens. The transverse resolution of OCM was 1 μm (since the back-aperture was underfilled) and the axial resolution was 2.9 μm in the immersion medium (limited by the spectral bandwidth of the OCM source).

Data acquisition. A custom LabVIEW acquisition software was used to acquire the data, with custom C-based programs to control the digitizer and the GPU modules. The software consists of three asynchronous modules. The first module generates the clocks, controls the motorized sample stages, handles the analog inputs for the SHG and CARS signals, and monitors for errors in the subsequent modules. The second asynchronous module controlled the digitizer and real-time display for FLIM, and the

third module for OCM acquisitions. Queue buffers were set up on LabVIEW to asynchronously pass each line from the digitizer memory to the GPU memory via the RAM for both FLIM and OCM. Separate streams on a single GPU (GeForce 2080 RTX, NVIDIA Corporation) were used for real-time processing of the photon counts to fluorescence lifetime values based on the algorithm described in Sorrells *et al.* [61,62] for each channel using phasor analysis and OCM reconstruction using matrix multiplication using the CUBLAS library. The fluorescence decay for each channel, the phasor components, the intensity, and the lifetime were saved for each channel as binary files. The raw OCM data and the analog input voltages (as 16-bit integers) were also saved in binary files. Custom MATLAB scripts were used to read in these images for generating the images displayed in the paper and for further analysis. A screenshot of the software is shown in Fig. S26 (Supplement 1).

Optical stimulation. An electronic shutter was placed in the detection path, which could be triggered with an external microcontroller (LabJack U12). The microcontroller was also used to control a fiber-based LED (470-nm, Thorlabs) pointed at the sample such that the turning on of the LED was synchronized to the closing of the shutter and vice versa.

Cell culture. The procedure for preparing the NE-4C cells was previously described in Iyer *et al.* [89]. The hippocampal neuronal culture was purchased as kits from (KTC57EDHP, Transnetyx by BrainBits) and the provided protocols were followed. The cells were grown on a No. 0 glass-bottomed imaging dish coated with Poly-D-Lysine (MakTek). The hippocampal cultures were transfected with CHETA-GFP (Addgene) by incubating it with $\sim 4 \times 10^{10}$ viral particles per imaging dish. The NE-4C cells were labelled with Calbryte 590AM by adding a working solution in DMSO and the cell medium of a dye for a final concentration of 100 nM per imaging dish and 1 μL for F125-Pluronic acid per imaging dish. The dye was washed off after 30 min of incubation with the neuronal culture external solution. Approximately 1 h before imaging, the NbActiv4 medium was replaced by the neuronal culture external solution prepared using the protocol described previously [90]. A stage top incubator (OkoLabs) was placed above the objective lens to ensure that the cells are maintained at 37°C with 5% CO_2 throughout their growth and during imaging.

The primary hippocampal neuronal cells transfected with CHETA-YFP [63] were imaged at 1.33 s per frame for 160 × 160 pixels with 640 incident laser pulses for each pixel. An electronic shutter was placed in the detection path, which could be triggered with an external microcontroller (LabJack). The microcontroller was also used to control a fiber-based LED (470-nm, Thorlabs) pointed at the sample such that the turning on of the LED was synchronized to the closing of the shutter and vice versa. Since the autofluorescence signals were weak for the primary neuronal model as well, the responses from an 8 × 8 superpixel were accumulated for the FLIM images.

Retinal imaging. All animal procedures were conducted in accordance with protocols approved by the Institutional Animal Care and Use Committee at the University of Illinois Urbana-Champaign. All experiments in this study were conducted in compliance with the ARRIVE guidelines. Freshly extracted retinae from a 3-month-old albino mouse following euthanasia by CO_2 asphyxiation were placed in imaging dishes with freshly prepared and pH balanced Ames' medium within a stage top incubator mimicking physiological conditions. The images were acquired at 0.3 Hz. A 470-nm LED (M470F1) was focused onto the sample over a circular region of 5-mm radius for a total power of 10 mW, triggered using a microcontroller (Lab Jack U12). The same controller was used to trigger the shutter placed in front of the HPDs to block the light to the detectors when the LED is turned on. Images were acquired over 1000 s with six optical excitations in between (10 s on time and 140 s between two excitation pulses).

For a more detailed analysis, the relative slopes were input as an N-dimensional feature vector for *k*-means clustering. The number of clusters varied between three and eight; the value of four was chosen because it was the maximum number of clusters where no two median responses in more than three channels had an absolute correlation coefficient greater than 0.5. The four clusters, therefore, yield four unique responses within the sample.

Brain imaging. The mice (3-month-old females) were euthanized with isoflurane overdose and decapitation, following which the brain was removed and placed in a cutting solution. The brain was sliced into 0.5-mm-thick slices and placed in an external solution for electrophysiology. The slices were placed in a stage-top incubator with physiological conditions (37°C and 5% CO_2). The slices were imaged within 1 h of extraction. The images were acquired in two different imaging conditions: high speed and high resolution. The high-speed images were acquired at 0.20 frames per second, and the high-resolution images were acquired at 0.055 frames per second, each spanning 200 × 200 μm. The same procedures described for the imaging and processing of the retina were used here for the brain. 25-μM glutamic acid (prepared by adding glutamic acid crystals to the external solution on the day of the experiment and preconditioned to physiological conditions in an incubator) was added to the dish at $t = 100$ s (for fast imaging) and $t = 300$ s (for high-resolution imaging).

B. Data Analysis

FLIM and SPEED. The ADQ7WB (Teledyne SP Devices) digitizer can sample at 5 GS/s for two channels and has an onboard open FPGA. While the acquisition clock operates at 5 GHz for two channels, the FPGA clock operates at 312.5 MHz. Therefore, 16 samples are available for processing at each falling edge of the FPGA. Since SPEED needs three consecutive samples for detecting the local peak, two 16-bit shift registers are set up as the memory to remember the last two samples from the previous cycle. Every clock cycle of the FPGA utilizes 18 consecutive 16-bit analog samples per channel to derive 16 instances of 4-bit photon counts. To maintain the same data size through the bus for the downstream modules of the FPGA (until the sample-skip module), four-packed copies of the photon counts are created such that the FPGA can be operated with a sample skip factor of four. The 16-bit photocurrents are converted to 4-bit photon counts leading to a 4× data compression factor.

SPEED, as seen in Fig. S3 (Supplement 1), relies on finding the local peaks by comparing each digitized sample to its nearest neighbors on either side and comparing it to photon thresholds (five thresholds for HPD, two threshold values for PMT). If both conditions are satisfied, *N* photons (depending on the threshold) are assumed to have arrived at that sampling instant. After this, the photons within each laser period are coherently aligned and summed for all laser pulses in a pixel (for the 80-MHz setup with hundreds of pulses per pixel) or a single line in a frame (for setups with lower repetition rates). The laser pulse is assumed to have

occurred at the peak of this summed decay profile. All photons are aligned to this inferred laser pulse digitally and cumulated across the response of all laser pulses for the pixel and across frames to build the histogram for fluorescence decay. The lifetime values can be estimated using a curve fitting to an exponential or using phasor analysis [91]. The latter was used throughout this paper and was performed in real-time on a GPU.

Since the photon counts from neurons were weak, the decays from each pixel were binned for 8×8 superpixels and used to derive the intensity and lifetime values. Each pixel in the sample had approximately two to 10 fluorescent photons and the binning size was chosen to ensure sufficient photons for lifetime estimation in each super-pixel. The intensity and lifetime values from any superpixel with fewer than 70 photons were rejected for all further analysis. The MATLAB functions corrcoef(), pca(), kmeans(), and fit(. . . ,. . . ,"poly2") were used for correlation coefficient calculation, for principal component analysis, for *k*-means clustering, and for fitting, respectively. The NAD(P)H and FAD intensities were normalized to the average intensity of each frame. The Ca^{2+} dynamics were also normalized by subtracting and dividing by the average fluorescence intensity of the superpixel during the first 20 frames.

OCM processing. The supercontinuum-based OCT/OCM system had artifacts along the axial direction not corrected by traditional methods of OCT/OCM image reconstructions. Since existing algorithms were insufficient to correct this dispersion mismatch, a solution called DISCOTECA (dispersion correction techniques for evident chromatic anomaly) was devised, which also provided a universal paradigm for OCT/OCM reconstruction. This algorithm is detailed in Iyer *et al.* [92].

Processing retinal imaging data. Since the average photon counts of the NAD(P)H and FAD channels were less than two photons per frame, all quantitative metrics were calculated after binning 16×16 pixels with an 8-pixel overlap; a minimum of 1000 photons were used for calculating the fluorescence lifetime values. The birefringence images were binned using a circular mean algorithm. For 50 s after each optical excitation, the responses collected from each superpixel for each contrast were fit to a first-order polynomial function. The relative slope for each contrast following each stimulation was used as the input to a *k*-means clustering algorithm. The median responses of each cluster were visualized. All intensity values were normalized to the median intensity of each superpixel across all 1000 s before clustering. The value of *k* was chosen such that no two clusters had an absolute correlation coefficient greater than 0.7.

Processing brain imaging data. Instead of calculating the slopes and intercepts after each excitation pulse, the slopes and intercepts were calculated for every 120-s duration.

Funding. Air Force Office of Scientific Research (FA9550-17-1-0387); National Eye Institute (R01EY029397); National Cancer Institute (R01CA241618); National Institute of Biomedical Imaging and Bioengineering (P41EB031772, R01EB028615, T32EB019944).

Acknowledgment. The authors would like to thank Jiho Kahng for assisting with the cells and Dr. Anita Mahadevan-Jansen for suggesting the source for the cell culture model. The authors also thank Dr. Guillermo Monroy for his assistance in naming VAMPIRE microscopy. The authors would also like to thank Dr. Marina Marjanovic and Dr. Edita Aksamitiene for their assistance in coordinating and executing this study. Additional information can be found in Ref. [93].

Disclosures. The technology for Raman microscopy using the pulse shaper and the photon counting technique for fast FLIM have been disclosed as intellectual properties to the Office of Technology Management at the University of Illinois Urbana-Champaign. The authors declare no other conflicts of interest.

Data availability. The raw data that support the findings of this study are available from the corresponding author upon request and through a collaborative research agreement. The codes used to acquire and process the images are available in Ref. [94].

Supplemental document. See Supplement 1 for supporting content.

REFERENCES

1. T. Akkin, D. Landowne, and A. Sivaprakasam, "Optical coherence tomography phase measurement of transient changes in squid giant axons during activity," J. Membr. Biol. **231**, 35–46 (2009).
2. Y. Yang, X.-W. Liu, H. Wang, *et al.*, "Imaging action potential in single mammalian neurons by tracking the accompanying sub-nanometer mechanical motion," ACS Nano **12**, 4186–4193 (2018).
3. K. M. Carter, J. S. George, and D. M. Rector, "Simultaneous birefringence and scattered light measurements reveal anatomical features in isolated crustacean nerve," J. Neurosci. Methods **135**, 9–16 (2004).
4. C. W. Shuttleworth, A. M. Brennan, and J. A. Connor, "NAD(P)H fluorescence imaging of postsynaptic neuronal activation in murine hippocampal slices," J. Neurosci. **23**, 3196–3208 (2003).
5. K. A. Kasischke, H. D. Vishwasrao, P. J. Fisher, *et al.*, "Neural activity triggers neuronal oxidative metabolism followed by astrocytic glycolysis," Science **305**, 99–103 (2004).
6. T. S. Blacker and M. R. Duchen, "Investigating mitochondrial redox state using NADH and NADPH autofluorescence," Free Radical Biol. Med. **100**, 53–65 (2016).
7. G. Pekkurnaz and X. Wang, "Mitochondrial heterogeneity and homeostasis through the lens of a neuron," Nat. Metab. **4**, 802–812 (2022).
8. J. G. Jackson and M. B. Robinson, "Regulation of mitochondrial dynamics in astrocytes: mechanisms, consequences, and unknowns," Glia **66**, 1213–1234 (2018).
9. C. M. Díaz-García, R. Mongeon, C. Lahmann, *et al.*, "Neuronal stimulation triggers neuronal glycolysis and not lactate uptake," Cell Metab. **26**, 361 (2017).
10. L. Pellerin, A. Bouzier-Sore, A. Aubert, *et al.*, "Activity-dependent regulation of energy metabolism by astrocytes: an update," Glia **55**, 1251–1262 (2007).
11. A. Schousboe, S. Scafidi, L. K. Bak, *et al.*, "Glutamate metabolism in the brain focusing on astrocytes," in *Glutamate and ATP at the Interface of Metabolism and Signaling in the Brain*, V. Parpura, A. Schousboe, and A. Verkhratsky, eds., Vol. **11** of Advances in Neurobiology (Springer International Publishing, 2014), pp. 13–30.
12. A. Bringmann, T. Pannicke, B. Biedermann, *et al.*, "Role of retinal glial cells in neurotransmitter uptake and metabolism," Neurochem. Int. **54**, 143–160 (2009).
13. N. R. Sibson, A. Dhankhar, G. F. Mason, *et al.*, "Stoichiometric coupling of brain glucose metabolism and glutamatergic neuronal activity," Proc. Natl. Acad. Sci. USA **95**, 316–321 (1998).
14. T. Amédée, A. Robert, and J. A. Coles, "Potassium homeostasis and glial energy metabolism," Glia **21**, 46–55 (1997).
15. S. Li and Z.-H. Sheng, "Energy matters: presynaptic metabolism and the maintenance of synaptic transmission," Nat. Rev. Neurosci. **23**, 4–22 (2022).
16. G. A. N. Gowda and D. Djukovic, "Overview of mass spectrometry-based metabolomics: opportunities and challenges," in *Mass Spectrometry in Metabolomics*, D. Raftery, ed., Methods in Molecular Biology (Springer New York, 2014), Vol. **1198**, pp. 3–12.
17. H. Li, M. Uittenbogaard, L. Hao, *et al.*, "Clinical insights into mitochondrial neurodevelopmental and neurodegenerative disorders: their biosignatures from mass spectrometry-based metabolomics," Metabolites **11**, 233 (2021).
18. F. R. Sharp and T. S. Kilduff, "The 2-deoxyglucose neuroanatomical mapping technique," Trends Neurosci. **4**, 144–148 (1981).
19. A. A. Fung and L. Shi, "Mammalian cell and tissue imaging using Raman and coherent Raman microscopy," WIREs Mech. Dis. **12**, e1501 (2020).

20. V. P. Bindokas, J. Jordán, C. C. Lee, *et al.*, "Superoxide production in rat hippocampal neurons: selective imaging with hydroethidine," J. Neurosci. **16**, 1324–1336 (1996).
21. K. M. Robinson, M. S. Janes, M. Pehar, *et al.*, "Selective fluorescent imaging of superoxide *in vivo* using ethidium-based probes," Proc. Natl. Acad. Sci. USA **103**, 15038–15043 (2006).
22. J. Wang, H. Fröhlich, F. B. Torres, *et al.*, "Mitochondrial dysfunction and oxidative stress contribute to cognitive and motor impairment in FOXP1 syndrome," Proc. Natl. Acad. Sci. USA **119**, e2112852119 (2022).
23. B. N. Lizama-Manibusan, S. Klein, J. R. McKenzie, *et al.*, "Analysis of a nitroreductase-based hypoxia sensor in primary neuronal cultures," ACS Chem. Neurosci. **7**, 1188–1191 (2016).
24. R. Cao, H. Wallrabe, and A. Periasamy, "Multiphoton FLIM imaging of NAD(P)H and FAD with one excitation wavelength," J. Biomed. Opt. **25**, 014510 (2020).
25. V. V. Ghukasyan and A. A. Heikal, eds., *Natural Biomarkers for Cellular Metabolism: Biology, Techniques, and Applications*, Series in Cellular and Clinical Imaging (CRC Press, 2017).
26. T. S. Blacker and M. R. Duchen, "Characterizing metabolic states using fluorescence lifetime imaging microscopy (FLIM) of NAD(P)H," in *Techniques to Investigate Mitochondrial Function in Neurons*, S. Strack and Y. M. Usachev, eds., Neuromethods (Springer New York, 2017), Vol. **123**, pp. 133–150.
27. W. Becker, A. Bergmann, R. Suarez Ibarrola, *et al.*, "Metabolic imaging by simultaneous FLIM of NAD(P)H and FAD," in *Multiphoton Microscopy in the Biomedical Sciences XIX*, A. Periasamy, P. T. So, and K. König, eds. (SPIE, 2019), p. 10.
28. S. You, H. Tu, E. J. Chaney, *et al.*, "Intravital imaging by simultaneous label-free autofluorescence-multiharmonic microscopy," Nat. Commun. **9**, 2125 (2018).
29. M. A. Yaseen, J. Sutin, W. Wu, *et al.*, "Fluorescence lifetime microscopy of NADH distinguishes alterations in cerebral metabolism *in vivo*," Biomed. Opt. Express **8**, 2368–2385 (2017).
30. A. J. Bower, C. Renteria, J. Li, *et al.*, "High-speed label-free two-photon fluorescence microscopy of metabolic transients during neuronal activity," Appl. Phys. Lett. **118**, 081104 (2021).
31. A. Aubert, L. Pellerin, P. J. Magistretti, *et al.*, "A coherent neurobiological framework for functional neuroimaging provided by a model integrating compartmentalized energy metabolism," Proc. Natl. Acad. Sci. USA **104**, 4188–4193 (2007).
32. K. C. Reinert, R. L. Dunbar, W. Gao, *et al.*, "Flavoprotein autofluorescence imaging of neuronal activation in the cerebellar cortex *in vivo*," J. Neurophysiol. **92**, 199–211 (2004).
33. L. Yang, R. R. Iyer, J. E. Sorrells, *et al.*, "Temporally optimized and spectrally shaped hyperspectral coherent anti-Stokes Raman scattering microscopy," Opt. Express **32**, 11474–11490 (2024).
34. J. E. Sorrells, L. Yang, R. R. Iyer, *et al.*, "Programmable hyperspectral coherent anti-Stokes Raman scattering microscopy," Opt. Lett. **49**, 2513–2516 (2024).
35. N. K. Howell, G. Arteaga, S. Nakai, *et al.*, "Raman spectral analysis in the C-H stretching region of proteins and amino acids for investigation of hydrophobic interactions," J. Agric. Food Chem. **47**, 924–933 (1999).
36. M. Osetrova, A. Tkachev, W. Mair, *et al.*, "Lipidome atlas of the adult human brain," Nat. Commun. **15**, 4455 (2024).
37. T. Akkin, C. Joo, and J. F. de Boer, "Depth-resolved measurement of transient structural changes during action potential propagation," Biophys. J. **93**, 1347–1353 (2007).
38. T. Akkin, D. Landowne, and A. Sivaprakasam, "Detection of neural action potentials using optical coherence tomography: intensity and phase measurements with and without dyes," Front. Neuroenerg. **2**, 22 (2010).
39. U. Baran and R. K. Wang, "Review of optical coherence tomography based angiography in neuroscience," Neurophotonics **3**, 010902 (2016).
40. Y. Chen, A. D. Aguirre, L. Ruvinskaya, *et al.*, "Optical coherence tomography (OCT) reveals depth-resolved dynamics during functional brain activation," J. Neurosci. Methods **178**, 162–173 (2009).
41. B. W. Graf, T. S. Ralston, H.-J. Ko, *et al.*, "Detecting intrinsic scattering changes correlated to neuron action potentials using optical coherence imaging," Opt. Express **17**, 13447–13457 (2009).
42. M. Lazebnik, D. L. Marks, K. Potgieter, *et al.*, "Functional optical coherence tomography for detecting neural activity through scattering changes," Opt. Lett. **28**, 1218–1220 (2003).
43. X. Li, M. A. Krol, S. Jahani, *et al.*, "Brain correlates of motor complexity during observed and executed actions," Sci. Rep. **10**, 10965 (2020).
44. T. Son, B. Wang, D. Thapa, *et al.*, "Optical coherence tomography angiography of stimulus evoked hemodynamic responses in individual retinal layers," Biomed. Opt. Express **7**, 3151 (2016).
45. G. Strangman, D. A. Boas, and J. P. Sutton, "Non-invasive neuroimaging using near-infrared light," Biol. Psychiatry **52**, 679–693 (2002).
46. Y.-J. Yeh, A. J. Black, D. Landowne, *et al.*, "Optical coherence tomography for cross-sectional imaging of neural activity," Neurophotonics **2**, 035001 (2015).
47. Y. Zhang, L. Yao, F. Yang, *et al.*, "INS-fOCT: a label-free, all-optical method for simultaneously manipulating and mapping brain function," Neurophotonics **7**, 015014 (2020).
48. R. A. Stepnoski, A. LaPorta, F. Raccuia-Behling, *et al.*, "Noninvasive detection of changes in membrane potential in cultured neurons by light scattering," Proc. Natl. Acad. Sci. USA **88**, 9382–9386 (1991).
49. S. Batabyal, S. Satpathy, L. Bui, *et al.*, "Label-free optical detection of action potential in mammalian neurons," Biomed. Opt. Express **8**, 3700 (2017).
50. B. Hill, E. Schubert, M. Nokes, *et al.*, "Laser interferometer measurement of changes in crayfish axon diameter concurrent with action potential," Science **196**, 426–428 (1977).
51. P. Marquet, C. Depeursinge, and P. J. Magistretti, "Review of quantitative phase-digital holographic microscopy: promising novel imaging technique to resolve neuronal network activity and identify cellular biomarkers of psychiatric disorders," Neurophotonics **1**, 020901 (2014).
52. C. Hu, R. Sam, M. Shan, *et al.*, "Optical excitation and detection of neuronal activity," J. Biophotonics **12**, e201800269 (2019).
53. C. Larivière-Loiselle, E. Bélanger, and P. Marquet, "Polychromatic digital holographic microscopy: a quasicoherent-noise-free imaging technique to explore the connectivity of living neuronal networks," Neurophotonics **7**, 040501 (2020).
54. T. Ling, K. C. Boyle, G. Goetz, *et al.*, "Full-field interferometric imaging of propagating action potentials," Light Sci. Appl. **7**, 107 (2018).
55. A. H. Badreddine, T. Jordan, and I. J. Bigio, "Real-time imaging of action potentials in nerves using changes in birefringence," Biomed. Opt. Express **7**, 1966 (2016).
56. M. Koike-Tani, T. Tominaga, R. Oldenbourg, *et al.*, "Instantaneous polarized light imaging reveals activity dependent structural changes of dendrites in mouse hippocampal slices," bioRxiv (2019).
57. R.-W. Lu, Q.-X. Zhang, and X.-C. Yao, "Circular polarization intrinsic optical signal recording of stimulus-evoked neural activity," Opt. Lett. **36**, 1866–1868 (2011).
58. A. J. Foust and D. M. Rector, "Optically teasing apart neural swelling and depolarization," Neuroscience **145**, 887–899 (2007).
59. K. König, "Multiphoton tomography for tissue engineering," Proc. SPIE **6858**, 68580C (2008).
60. L. Perrin, B. Bayarmagnai, and B. Gligorijevic, "Frontiers in intravital multiphoton microscopy of cancer," Cancer Rep. **3**, e1192 (2020).
61. J. E. Sorrells, R. R. Iyer, L. Yang, *et al.*, "Computational photon counting using multithreshold peak detection for fast fluorescence lifetime imaging microscopy," ACS Photonics **9**, 2748–2755 (2022).
62. J. E. Sorrells, R. R. Iyer, L. Yang, *et al.*, "Single-photon peak event detection (SPEED): a computational method for fast photon counting in fluorescence lifetime imaging microscopy," Opt. Express **29**, 37759–37775 (2021).
63. L. A. Gunaydin, O. Yizhar, A. Berndt, *et al.*, "Ultrafast optogenetic control," Nat. Neurosci. **13**, 387–392 (2010).
64. J. N. Cobley, M. L. Fiorello, and D. M. Bailey, "13 reasons why the brain is susceptible to oxidative stress," Redox Biol. **15**, 490–503 (2018).
65. D. Liu, M. Pitta, and M. P. Mattson, "Preventing NAD(+) depletion protects neurons against excitotoxicity: bioenergetic effects of mild mitochondrial uncoupling and caloric restriction," Ann. NY Acad. Sci. **1147**, 275–282 (2008).
66. N. Ma, M. A. Digman, L. Malacrida, *et al.*, "Measurements of absolute concentrations of NADH in cells using the phasor FLIM method," Biomed. Opt. Express **7**, 2441–2452 (2016).
67. J. C. Walton, B. Selvakumar, Z. M. Weil, *et al.*, "Neuronal nitric oxide synthase and NADPH oxidase interact to affect cognitive, affective, and social behaviors in mice," Behav. Brain Res. **256**, 320–327 (2013).
68. R. C. Stanton, "Glucose-6-phosphate dehydrogenase, NADPH, and cell survival," IUBMB Life **64**, 362–369 (2012).

69. S. K. McCann and C. L. Roulston, "NADPH oxidase as a therapeutic target for neuroprotection against ischaemic stroke: future perspectives," Brain Sci. **3**, 561–598 (2013).
70. M. Wong-Riley, "Energy metabolism of the visual system," Eye Brain **2**, 99–116 (2010).
71. D.-Y. Yu, S. J. Cringle, C. Balaratnasingam, *et al.*, "Retinal ganglion cells: Energetics, compartmentation, axonal transport, cytoskeletons and vulnerability," Prog. Retinal Eye Res. **36**, 217–246 (2013).
72. R. M. Andrews, P. G. Griffiths, M. A. Johnson, *et al.*, "Histochemical localisation of mitochondrial enzyme activity in human optic nerve and retina," Br. J. Ophthalmol. **83**, 231–235 (1999).
73. H. Liu and V. Prokosch, "Energy metabolism in the inner retina in health and glaucoma," Int. J. Mol. Sci. **22**, 3689 (2021).
74. T. Zhao, Z. D. Chiang, J. W. Morriss, *et al.*, "Spatial genomics enables multi-modal study of clonal heterogeneity in tissues," Nature **601**, 85–91 (2022).
75. H. Murali Mahadevan, A. Hashemiaghdam, G. Ashrafi, *et al.*, "Mitochondria in neuronal health: from energy metabolism to Parkinson's disease," Adv. Biol. **5**, 2100663 (2021).
76. X.-H. Zhu, M. Lu, B.-Y. Lee, *et al.*, "*In vivo* NAD assay reveals the intracellular NAD contents and redox state in healthy human brain and their age dependences," Proc. Natl. Acad. Sci. USA **112**, 2876–2881 (2015).
77. K. A. Anderson, A. S. Madsen, C. A. Olsen, *et al.*, "Metabolic control by sirtuins and other enzymes that sense NAD+, NADH, or their ratio," Biochimica Biophysica Acta **1858**, 991–998 (2017).
78. R. R. Iyer, J. E. Sorrells, K. K. D. Tan, *et al.*, "Analog multiplexing of a laser clock and computational photon counting for fast fluorescence lifetime imaging microscopy," Biomed. Opt. Express **15**, 2048–2062 (2024).
79. T. D. Payne, A. S. Moody, A. L. Wood, *et al.*, "Raman spectroscopy and neuroscience: from fundamental understanding to disease diagnostics and imaging," Analyst **145**, 3461–3480 (2020).
80. L. Yang, R. R. Iyer, J. E. Sorrells, *et al.*, "Label-free multimodal polarization-sensitive optical microscope for multiparametric quantitative characterization of collagen," Optica **11**, 155–165 (2024).
81. L. Sacconi, D. A. Dombeck, and W. W. Webb, "Overcoming photodamage in second-harmonic generation microscopy: real-time optical recording of neuronal action potentials," Proc. Natl. Acad. Sci. USA **103**, 3124–3129 (2006).
82. L. K. Wareham, R. O. Baratta, B. J. Del Buono, *et al.*, "Collagen in the central nervous system: contributions to neurodegeneration and promise as a therapeutic target," Mol. Neurodegener. **19**, 11 (2024).
83. Y. Zhao, B. W. Graf, E. J. Chaney, *et al.*, "Integrated multimodal optical microscopy for structural and functional imaging of engineered and natural skin," J. Biophotonics **5**, 437–448 (2012).
84. J. Ryu, U. Kang, J. W. Song, *et al.*, "Multimodal microscopy for the simultaneous visualization of five different imaging modalities using a single light source," Biomed. Opt. Express **12**, 5452–5469 (2021).
85. F. Crisafi, V. Kumar, A. Perri, *et al.*, "Multimodal nonlinear microscope based on a compact fiber-format laser source," Spectrochim. Acta Part A **188**, 135–140 (2018).
86. T. Lee, R. P. Trivedi, and I. I. Smalyukh, "Multimodal nonlinear optical polarizing microscopy of long-range molecular order in liquid crystals," Opt. Lett. **35**, 3447–3449 (2010).
87. H. Chen, H. Wang, M. N. Slipchenko, *et al.*, "A multimodal platform for nonlinear optical microscopy and microspectroscopy," Opt. Express **17**, 1282–1290 (2009).
88. H. Tu, Y. Liu, D. Turchinovich, *et al.*, "Stain-free histopathology by programmable supercontinuum pulses," Nat. Photonics **10**, 534–540 (2016).
89. R. R. Iyer, J. E. Sorrells, L. Yang, *et al.*, "Label-free metabolic and structural profiling of dynamic biological samples using multimodal optical microscopy with sensorless adaptive optics," Sci. Rep. **12**, 3438 (2022).
90. C. Renteria, Y.-Z. Liu, E. J. Chaney, *et al.*, "Dynamic tracking algorithm for time-varying neuronal network connectivity using wide-field optical image video sequences," Sci. Rep. **10**, 2540 (2020).
91. M. A. Digman, V. R. Caiolfa, M. Zamai, *et al.*, "The phasor approach to fluorescence lifetime imaging analysis," Biophys. J. **94**, L14–L16 (2008).
92. R. R. Iyer, L. Yang, J. E. Sorrells, *et al.*, "Dispersion mismatch correction for evident chromatic anomaly in low coherence interferometry," APL Photonics **9**, 076114 (2024).
93. "Biophotonics imaging laboratory," https://biophotonics.illinois.edu.
94. R. R. Iyer, J. Sorrells, L. Yang, *et al.*, "Code to generate reconstruction matrix for SDOCM," Zenodo (2024), https://doi.org/10.5281/zenodo.13544776.